Wiley Analytical Science

Specific Heat Capacity Determination by DSC

April 19, 10:00am - 11:00am EDT

Specific heat capacity (cp) is an important, temperature-dependent material property and is often specified in material data sheets. It is a key property for improving technical processes such as injection molding, spray drying, or crystallization, as well as for the safety analysis of chemical processes and the design of chemical reactors.

Watch this session during the WAS Virtual Conference:

Dr. Jürgen Schawe

Register Now

This talk is sponsored by **METTLER TOLEDO**

Generation of Free Carriers in MoSe₂ Monolayers Via Energy Transfer from CsPbBr₃ Nanocrystals

Aswin Asaithambi, Nastaran Kazemi Tofighi, Nicola Curreli, Manuela De Franco,
Aniket Patra, Nicolò Petrini, Dmitry Baranov, Liberato Manna, Francesco Di Stasio,
and Ilka Kriegel*

Transition metal dichalcogenide (TMDCs) monolayers make an excellent component in optoelectronic devices such as photodetectors and phototransistors. Selenide-based TMDCs, specifically molybdenum diselenide (MoSe₂) monolayers with low defect densities, show much faster photoresponses compared to their sulfide counterpart. However, the typically low absorption of the atomically thin MoSe₂ monolayer and high exciton binding energy limit the photogeneration of charge carriers. Yet, integration of light-harvesting materials with TMDCs can produce increased photocurrents via energy transfer. In this article, it is demonstrated that the interaction of cesium lead bromide (CsPbBr₃) nanocrystals with MoSe₂ monolayers results into an energy transfer efficiency of over 86%, as ascertained from the quenching and decay dynamics of the CsPbBr₃ nanocrystals emission. Notably, the increase in the MoSe₂ monolayer emission in the heterostructure accounts only for 33% of the transferred energy. It is found that part of the excess energy generates directly free carriers in the MoSe₂ monolayer, as a result of the transfer of energy into the exciton continuum. The efficiency of the heterostructure via enhanced photocurrents with respect to the single material unit is proven. These results demonstrate a viable route to overcome the high exciton binding energy typical for TMDCs, as such having an impact on optoelectronic processes that rely on efficient exciton dissociation.

1. Introduction

The family of transition metal dichalcogenides (TMDCs) crystals is a class of van der Waals materials with a layered structure.[1] They are an attractive component in semiconductor devices thanks to their outstanding electronic, mechanical, optical, thermal, and chemical properties at the monolayer level.[2–6] They also show excellent in-plane carrier mobility, high quantum efficiency, and the indirect to direct bandgap crossover approaching the monolayer thickness, which favors light-matter interaction.[1,7,8] In particular, two-dimensional (2D) molybdenum diselenide (MoSe₂) shows a bandgap (E_g) of ≈1.55 eV, which is close to the optimal bandgap value of single-junction solar cells and photo-electrochemical devices.[9,10] For these reasons, MoSe₂ is a competitive candidate for applications in electronics and photonics. However, the realization of MoSe₂-based optoelectronic devices is limited by their weak optical absorption

A. Asaithambi, N. Kazemi Tofighi, N. Curreli, N. Petrini, I. Kriegel
Functional Nanosystems
Istituto Italiano di Tecnologia
Via Morego 30, Genova 16163, Italy
E-mail: ilka.kriegel@iit.it

M. De Franco, F. D. Stasio
Photonic Nanomaterials
Istituto Italiano di Tecnologia
Via Morego 30, Genoa 16163, Italy

M. De Franco
Dipartimento di Chimica e Chimica Industriale
Università
Degli Studi di Genova
Via Dodecaneso 31, Genoa 16146, Italy

A. Patra
Optoelectronics
Istituto Italiano di Tecnologia
Via Morego 30, Genoa 16163, Italy

A. Patra
Dipartimento di Fisica
Universitá della Calabria
Rende 87036, Italy

N. Petrini
Dipartimento di Fisica
Università degli Studi di Genova
Via Dodecaneso 33, Genova 16146, Italy

D. Baranov, L. Manna
Nanochemistry Department
Istituto Italiano di Tecnologia
Via Morego 30, Genoa 16163, Italy

in the visible spectra range and consequently low generation of carriers in the atomically thin layer.[11,12] Additionally, quantum confinement effects and reduced Coulomb screening give rise to large exciton binding energies of around 100 meV, preventing the spontaneous or thermally induced dissociation of the exciton into free charges.[13] This effect is detrimental for various optoelectronic applications, such as the generation of photocurrent, which rely on the efficient dissociation of excitons.[13]

The coupling of light-harvesting materials that can transfer the absorbed light energy to the TMDC crystals, represents an interesting route to overcome the abovementioned limitations. The key process involved in finding suitable materials for the design and manufacture of such hybrid optoelectronic devices is the efficient transfer of energy and/or charge at the interface. Several low-dimensional light-harvesting materials such as colloidal quantum dots, perovskites, nanowires, and other layered materials have been integrated with TMDCs.[14–19] Among them, cesium lead bromide ($CsPbBr_3$) nanocrystals represent an emerging class of materials with excellent visible light absorption, high defect tolerance, long carrier diffusion length, and size-dependent electronic properties, showing an E_g of ≈2.4 eV.[16] In fact, in initial works, the interaction between $CsPbBr_3$ and Se-based TMDCs was studied. For example, Zhang et al.[14] demonstrated near-unity energy transfer efficiency between bulk $CsPbBr_3$ and WSe_2 and Hassan et al.[20] reported an enhanced photocurrent in a $CsPbBr_3$ nanocrystals and $MoSe_2$ nanosheets hybrid.

In this article, we show that the coupling of colloidal $CsPbBr_3$ nanocrystals with $MoSe_2$ monolayers results in an energy transfer efficiency of more than 86%, supported by optical measurements of emission quenching/enhancement and carrier lifetime. Importantly, we found that the transferred energy from $CsPbBr_3$ nanocrystals to $MoSe_2$ monolayers results in the direct generation of free carriers in $MoSe_2$ monolayers, with a 33% increase in the free carrier density compared to pristine $MoSe_2$ monolayers. Only a fraction of the generated free carriers recombines radiatively. This indicates a novel route to overcome the strong exciton binding energy of monolayer TMDCs by exploiting energy transfer to the exciton continuum of the TMDC. Our findings are supported by an order of magnitude (nA to sub-μA) increase in the photocurrent of the $CsPbBr_3/MoSe_2$ heterostructure with respect to the pristine $MoSe_2$ monolayers.

2. Results and Discussion

We prepared stable $CsPbBr_3$ nanocrystals (P-NCs) passivated with didodecyldimethylammonium bromide (DDAB) as a ligand using methods previously developed in our groups (also described in the Methods section in the Supporting Information).[21,22] **Figure 1**a shows the scanning electron microscope (SEM) image of a uniform single layer of P-NCs on a Si/SiO_2 substrate. As synthesized P-NCs have a size distribution of ≈7.2 ± 0.8 nm (transmission electron microscope (TEM) image and size
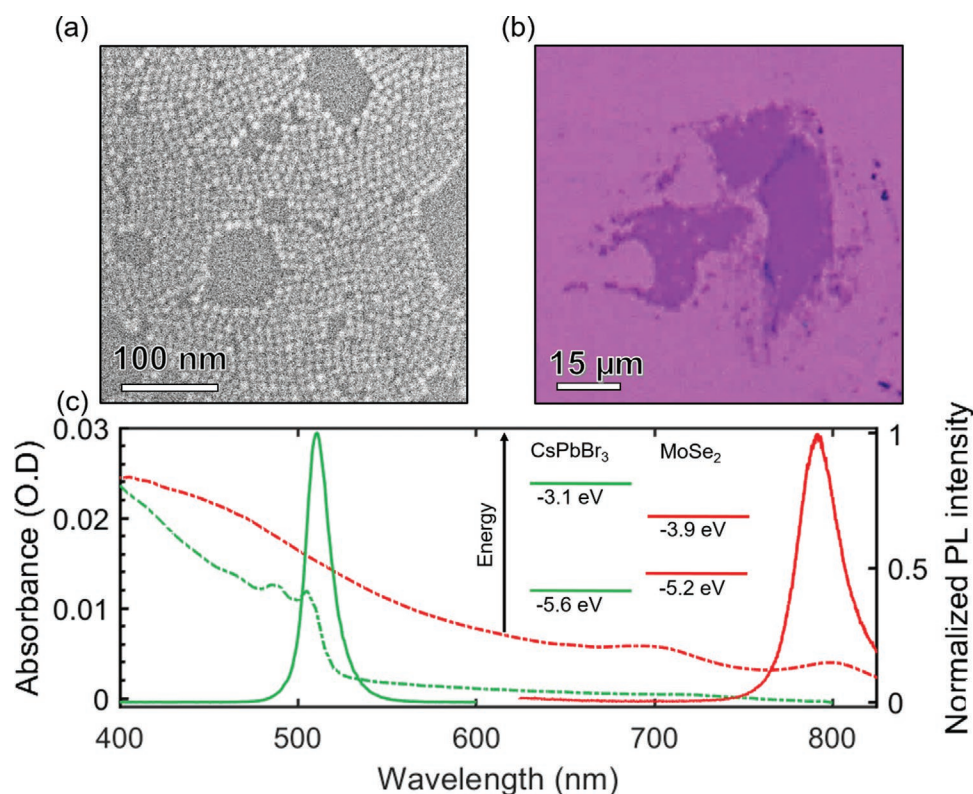

Figure 1. a) Scanning electron microscope (SEM) image of uniform P-NCs on Si/SiO_2 substrate. b) Optical micrograph of exfoliated ML-$MoSe_2$. c) Absorption spectra (in dashed curve) of P-NC (green), ML-$MoSe_2$ (red) and PL spectra (solid curve) of P-NC (green), ML-$MoSe_2$ (red), Schematic of type I band alignment of P-NC and ML-$MoSe_2$ shown in inset.

distribution analysis shown in Figure S1a,b). The MoSe$_2$ monolayers (ML-MoSe$_2$) were prepared using the Au-assisted exfoliation technique (see Methods in Supporting Information), which enables the fabrication of large-area samples ranging from a few to hundreds of micrometers.[23–25] The optical micrograph of an exfoliated monolayer is shown in Figure 1b. As-synthesized colloidal P-NC films were fabricated via spin coating, resulting in nearly monolayer films, as characterized by SEM (Figure 1a). We first characterized the bare P-NC films using optical absorption and photoluminescence spectroscopy. The P-NCs exhibit an exciton peak absorption at 505 nm and an emission maximum at 515 nm (Figure 1c). Emission at 515 nm is close to the bulk CsPbBr$_3$ emission wavelength (maximum at 525 nm)[26] indicating weak confinement in P-NCs. The absorption spectrum of ML-MoSe$_2$ shown in Figure 1c was calculated using Beer–Lambert law from the absorption coefficient spectrum taken from the literature.[27] The PL spectrum of ML-MoSe$_2$ was measured in a μ-PL system and is displayed in Figure 1c, evidencing a maximum PL around 800 nm. An overlap of the emission of the P-NC and the absorption of ML-MoSe$_2$ is observed, which represents a prerequisite for efficient energy transfer between P-NC and ML-MoSe$_2$ crystals. The valence band maximum energy (E_{VBM}) of −5.6 eV and the conduction band minimum energy (E_{CBM}) of −3.1 eV of the P-NCs were taken from a previous report for the same type of P-NCs.[21] The calculated E_{VBM} and E_{CBM} of −3.9 and −5.2 eV of ML-MoSe$_2$ were taken from a previous report.[28] Together, P-NC and ML-MoSe$_2$ form a type I band alignment, as depicted in Figure 1c.

The fabrication of the CsPbBr$_3$/MoSe$_2$ heterostructure (HET) was carried out via spin-coating of the P-NCs on top of the ML-MoSe$_2$. Upon spin coating, the P-NCs form a monolayer on top of both, substrate and ML-MoSe$_2$, as shown in the schematic in **Figure 2**a. This is confirmed by SEM, where a monolayer of P-NCs (solution concentration: 2 mg mL^{-1}) is observed on top of ML-MoSe$_2$ and the substrate, as shown in Figure 2b. Figure 2c shows a fluorescence microscopy image of P-NC emission intensity distribution in the HET acquired using a 400 nm laser excitation and a detection range of 480–550 nm. Notably, the P-NCs emission intensity on the ML-MoSe$_2$ (optical micrograph shown in Figure 1b) was significantly quenched compared to the bare P-NC emission on the substrate suggesting energy transfer from the P-NCs to the ML-MoSe$_2$.

To better quantify the emission characteristics and understand the physical origin of the quenching, we performed μ-PL spectroscopy (laser spot size of 1.7 μm) on P-NCs deposited on the ML-MoSe$_2$ (referred as HET) and on the substrate

only (P-NC). **Figure 3**a shows the steady-state μ-PL spectrum of P-NCs emission on substrate (in green) and the P-NCs emission in the HET (in black). Upon excitation with a 400 nm laser, we see PL from P-NCs around 515 nm, which gets quenched significantly when the P-NCs are placed on ML-MoSe$_2$. The ML-MoSe$_2$ emission instead is enhanced in the case of HET as shown in Figure 3b (ML-MoSe$_2$ emission spectrum on substrate in red and in HET in black). To be able to separate the monolayer ML-MoSe$_2$ PL from the perovskite P-NC PL, the former being orders of magnitude smaller, we diluted the P-NC film coupled to the ML-MoSe$_2$. We used 50 times diluted P-NCs sample and identified a sparse distribution of P-NCs on the substrate as well as on the ML-MoSe$_2$ (SEM image is given in Figure S2, Supporting Information). The corresponding absorption spectrum is given in Figure S3, Supporting Information. These three experimental observations, namely the overlapping of the P-NCs emission with the optical absorption of ML-MoSe$_2$ (Figure 1c), the quenching of the PL of P-NCs in the HET (Figure 3a), and the simultaneous enhancement in the ML-MoSe$_2$ PL (Figure 3b), suggest an energy transfer from the P-NCs to the ML-MoSe$_2$. The efficiency of energy transfer in the HET can be quantified from both donor (P-NC) quenching and acceptor (ML-MoSe$_2$) enhancement (statistics to the quantification are found in Figure S4, Supporting Information). If the energy transfer in the HET is the only process involved in the relaxation of the excited carriers besides spontaneous emission, we can calculate the efficiency from P-NC quenching using the following equation[29]:

$$\phi_{ET} = 1 - \frac{A_{P-NC}(\lambda_{exc})}{A_{HET}(\lambda_{exc}) - A_{ML-MoSe2}(\lambda_{exc})} \cdot \frac{I_{P-NC}}{I^0_{P-NC}} = 1 - \frac{I_{P-NC}}{I^0_{P-NC}} \tag{1}$$

where ϕ_{ET} is the efficiency of energy transfer (ET), and $A_{P-NC}(\lambda_{exc})$, $A_{HET}(\lambda_{exc})$, $A_{ML-MoSe2}(\lambda_{exc})$ are the absorbance of the P-NCs, the HET and the ML-MoSe$_2$ at the excitation wavelength (400 nm), respectively. The values of I^0_{P-NC} and I_{P-NC} are the integrated intensities of P-NC emission on the substrate and in the case of HET, respectively. We measured the value of $A_{P-NC}(\lambda_{exc})$ by spin-coating a uniform layer of P-NCs on fused silica, reproducing the same process used for the HET formation with the ML-MoSe$_2$ (absorbance spectrum shown in Figure 1c in dashed green). The absorbance of the ML-MoSe$_2$ ($A_{ML-MoSe2}(\lambda_{exc})$), at the excitation wavelength was calculated to be 0.245 using the Beer–Lambert law and the absorption coefficient taken from the literature.[27] Due to the presence of an isolating barrier (ligand: DDAB) between P-NCs and ML-MoSe$_2$
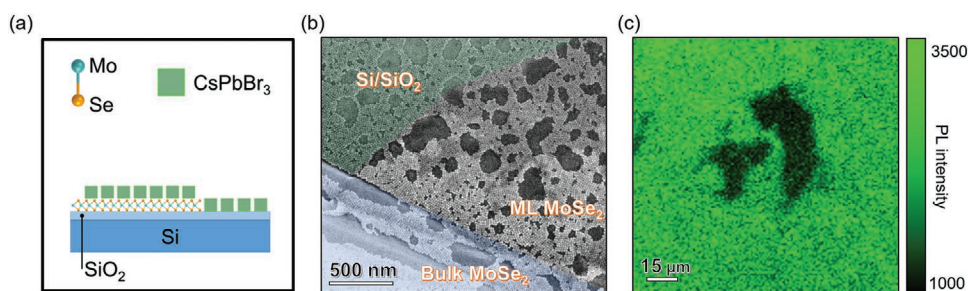

Figure 2. a) Schematic of the arrangement of P-NCs on ML-MoSe$_2$ and the substrate. b) SEM image of a film of P-NCs on ML-MoSe$_2$, bulk MoSe$_2$, and the Si/SiO$_2$ substrate. c) Confocal PL (480–550 nm) image of P-NCs on ML-MoSe$_2$ (dark region) and on Si/SiO$_2$ substrate (bright green emission).
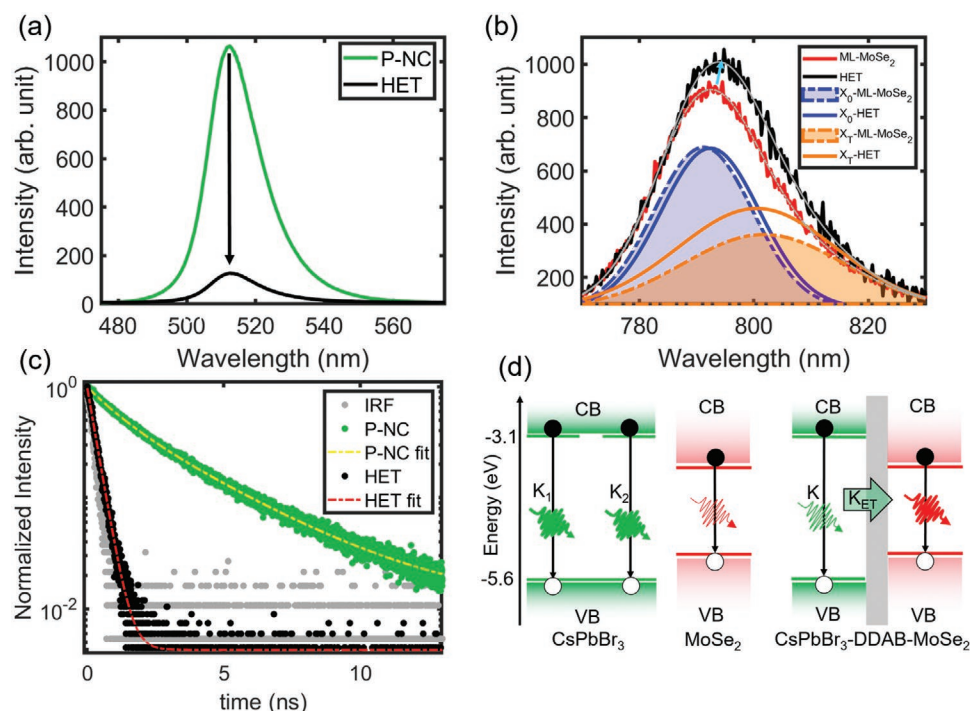
Figure 3. a) PL spectra of P-NCs in the HET (black) and on the substrate (green) excited with a 400 nm laser with an excitation power of 1 µW and 1s integration time. b) PL spectra of ML-MoSe$_2$ in the HET (black) and without P-NCs (red) excited with 400 nm laser with an excitation power of 60 µW and 10 s integration time. Both spectra have been deconvoluted into their contribution of the exciton (X_0, blue) and trion (X_T, orange) PL. c) PL emission decay of the P-NCs in the HET (black) and on the substrate (green). d) Schematic model depicting the major photoinduced processes in the single components (left) of CsPbBr$_3$ NCs (green) and MoSe$_2$ (red) and the HET (right). The grey shaded area illustrates the DDAB ligands that physically separate the two domains of the HET. The change in arrows' weight indicates the observed emission quenching and enhancement.

it is safe to assume zero ground state interaction, hence, $A_{HET}(\lambda_{exc})$ can be written as the sum of the absorbance of the individual materials.[30,31] All the values used in this calculation are shown in Table S1, Supporting Information. With this assumption, we can simplify Equation 1 in terms of integrated PL intensities of P-NCs on and off (substrate only) the HET.[32] Applying the equation for the PL spectra of P-NC emission, we calculate the ET efficiency to be 86%.

We further quantify the rate and efficiency of the exciton energy transfer from time-resolved µ-PL spectroscopy of P-NC emission on and off the HET. A 400 nm pulsed laser with a pulse width of 49.7 ps and a repetition rate of 10 MHz was used for excitation and P-NC PL was detected using an avalanche photo-diode (APD) connected to a time-correlated single-photon counting (TCSPC) system. The average PL lifetime in the case of ML-MoSe$_2$ is in the range of a few picoseconds, which is below the resolution of the TCSPC. Therefore, we calculated the rates from the P-NCs PL decay alone. Figure 3c shows the PL decay of P-NCs on the substrate (green, and the fit in dashed yellow) and in the HET (black, and the fit in dashed red). The P-NCs emission is characterized by a faster decay on the HET compared to the P-NCs on the substrate. The P-NCs emission on the substrate has a biexponential decay (see Equation S1, Supporting Information) with rates (K_1 and K_2) of 0.8×10^9 s^{-1} and 0.29×10^9 s^{-1} and amplitudes of 0.51 and 0.49, respectively (the respective time constants are given in Table S3, Supporting Information and Section 2, Supporting Information). In comparison, the PL decay of the P-NCs on the

HET displays a monoexponential (see Equation S3, Supporting Information) behavior, with a rate (K) of 4.16×10^9 s^{-1} and a lifetime of 0.24 ns. Since the decay of HET is close to the instrument response function of the system, the convoluted fit could still overestimate the time constant (τ_{HET}) and underestimate the energy transfer efficiency and rate. Therefore the estimated energy transfer rate and efficiency provide us with a lower limit and the real values are expected to be even larger. We calculate the amplitude average lifetime from the P-NCs PL decay on the substrate to be 2.8 ns (see Equation S2, Supporting Information).[33] There is an order of magnitude decrease in the excited state lifetime of the P-NCs when it is part of the HET. We then calculate the rate (K_{ET}) and the efficiency of ET using Equations 2 and 3:

$$K_{ET} = \frac{1}{\tau_{HET}} - \frac{1}{\tau_{P-NC}} \tag{2}$$

$$\phi_{ET} = 1 - \frac{\tau_{HET}}{\tau_{P-NC}} \tag{3}$$

Where τ_{P-NC} is the average lifetime of P-NC PL on the substrate and τ_{HET} is the average lifetime of P-NCs PL on the HET. We apply these formulae and calculate the ET rate to be 3.8×10^9 s^{-1} and ϕ_{ET} to be ≈92%. Notably, while the P-NC PL decay off the HET shows two different recombination rates, the P-NC emission on the HET shows a mono-exponential decay. The biexponential nature of the P-NC PL decay off the

**ADVANCED
SCIENCE NEWS**

www.advancedsciencenews.com

**ADVANCED
OPTICAL
MATERIALS**

www.advopticalmat.de

HET is typical for this type of material and is usually assigned to different defect-mediated recombination mechanisms.[34,35] The mono-exponential decay in the HET instead indicates a dominant ET, i.e., most of the excited state charge carriers irrespective of their origin lose their energy via the energy transfer process.

The efficiency of energy transfer can also be calculated from the acceptor PL. For an acceptor system with unity PL quantum yield, almost all the transferred energy should result in the enhancement of the acceptor PL. Therefore, the efficiency calculated from the enhancement should match the quenching efficiency of the donor. Using Equation 4, we calculate the ET efficiency from ML-MoSe$_2$ PL enhancement:

$$\phi_{ET} = \frac{A_{ML-MoSe2}(\lambda_{exc})}{A_{HET}(\lambda_{exc}) - A_{ML-MoSe2}(\lambda_{exc})} \left(\frac{I_{ML-MoSe2}}{I^0_{ML-MoSe2}} - 1\right) \qquad (4)$$

where $I^0_{ML-MoSe2}$ and $I_{ML-MoSe2}$ are the integrated PL intensities of ML-MoSe$_2$ off and on the HET respectively.[29] The value of A_{P-NC-} in the HET is taken from the absorption spectrum of the diluted NC film in Figure S3, Supporting Information. All the values used in this calculation are shown in Table S2, supporting information. Applying Equation 4, we calculate the ET efficiency to be 33%, implying an increased number of excitons in ML-MoSe$_2$. We want to remark that the quenching of P-NC PL, faster PL decay of P-NC, and the enhancement of ML-MoSe$_2$ PL are most probably a result of the Förster resonance energy transfer (FRET), due to the significant overlap in the emission of the donor (P-NC) and absorption of the acceptor (ML-MoSe$_2$) and the large separation distance between both due to the organic ligand (DDAB) passivation of the P-NC. A direct charge transfer from P-NC and ML-MoSe$_2$ is improbable due to the spatial barriers in the form of the DDAB.[36–38]

Figure 3d shows the two-particle energy level model that summarizes the results thus far: upon optical excitation of the P-NCs alone, we observe a strong PL with two different excited state populations that recombines at different rates. In the heterostructure, on the other hand, we observe ≈86% of exciton energy from P-NCs being transferred to the ML-MoSe$_2$. The nonradiative energy transfer reduces the PL lifetime of P-NC in the heterostructure to a fast monoexponential decay. The calculated efficiency from time-resolved data of 92% agrees well with the PL quenching data. The ET efficiency of 33% calculated from the enhancement of ML-MoSe$_2$ PL represents the increase in the number of excitons in ML-MoSe$_2$. Efficient quenching from P-NCs PL is evidence of energy transfer from P-NCs to ML-MoSe$_2$ upon excitation. The lower efficiency of PL enhancement in ML-MoSe$_2$ indicates that only a fraction of the transferred energy results in the formation of excitons with the subsequent emission of photons. The calculated efficiencies should be in agreement for the exclusive process of radiative recombination of the transferred energy in the heterostructure. The observed discrepancy indicates additional processes. In fact, when consulting the energy level alignment, it becomes obvious that the energy transferred from P-NCs to ML-MoSe$_2$ would most likely populate the continuum states far above the excitonic levels in ML-MoSe$_2$, hence into the generation of free carriers. Given the low quantum efficiency of TMDC monolayers in general (<6%) due to defects, band nesting (at high

energy excitation),[39] and exciton-exciton annihilation,[40] we assume that only a fraction of those free carriers recombines radiatively, accounting for the 33% efficiency calculated above. To further evaluate this, we investigated the PL spectra of the ML-MoSe$_2$. In 2D-TMDCs it is very well established that enhanced carrier density can be extracted by closely examining and deconvoluting the PL spectra into the spectral contribution of exciton and trion PL.[41] This is the result of the high binding energy of the trions (excitons that bind to a free carrier in the system) of >10 meV.[41–44] Therefore the trion contribution can be an indicator for the free carrier density in the ML-MoSe$_2$ even at room temperature.[41,45–49] The carrier density can be quantified by considering the thermal equilibrium between exciton (n_X), trion (n_T), and the free carrier density (n_e), which follows a Boltzmann distribution at low excitation densities.[50,51] This model, based on the law of mass action, is given in Equation S4, Supporting Information.

Assuming that the relative masses and the trion binding energy remain unchanged upon the addition of P-NCs, we can obtain the change in the trion-exciton (n_T/n_X) density ratio from the ML-MoSe$_2$ PL alone and in the HET by deconvoluting the PL into two Gaussian curves (See Section 3 in Supporting Information). The higher energy peak corresponds to exciton (x_0) and the other to trion (x_T) PL (see Figure 3b, blue and orange curves, respectively). Since the intensity ratio (I_T/I_X) is proportional to the trion-exciton density (n_T/n_X) ratio, the increase in the free carrier density results in a higher (I_T/I_X).[47] The co-existence of excitons, trions, and free carriers is typical for TMDCs. In fact, high excitation energies result into the generation of free carriers (electrons and holes), which bind to form excitons and other excitonic complex emissions, such as trions and biexcitons.[52–55] Such high-energy excitation process can be considered analogous to the energy transfer to the exciton continuum observed by us. We substitute the density ratio with the intensity ratio of trion-exciton (values given in Table S4, Supporting Information) on both ML-MoSe$_2$ and HET and calculate a relative increase of up to 33% in the free carrier density in the HET (see Figure 3b and Section 3 in the Supporting Information for details).

We summarize our results in a one-particle energy level model shown in **Figure 4**. For pristine ML-MoSe$_2$, upon photoexcitation the dominant species found are excitons (left panel in Figure 4). With the addition of P-NCs, we see an increase of 33% in the overall emission obtained from the optical studies. Together with the low quantum yield of ML-MoSe$_2$, our results, therefore, suggest that the ET from P-NCs to ML-MoSe$_2$ results in an increased number of free carriers rather than tightly bound excitons. In photoexcited TMDCs, excitons and free carriers can co-exist.[56] This increased free carrier density upon energy transfer is observed as an increased trion contribution to the spectrum (right panel in Figure 4). Hence, the route of energy transfer to the exciton continuum high above the excitonic states in the 2D-TMDC, represents an interesting route to generate directly free carriers in ML-MoSe$_2$. The additionally remaining energy that has been transferred but not detected by us, might be lost through other factors, such as the scattering of light from the top P-NCs layer.[15]

As a proof of principle, we performed photocurrent measurements on ML-MoSe$_2$ and HET. An external bias is applied
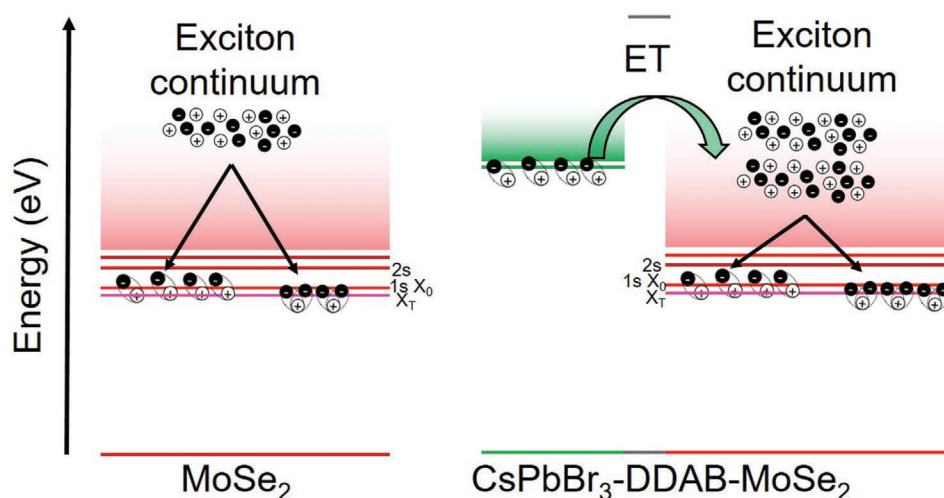
Figure 4. Schematic one particle energy level model of the heterostructure. Left: one particle picture of ML-MoSe$_2$ alone depicting the energy levels of excitons (x_0) in the 1S and 2S states and the trions (x_T). The exciton continuum is given above. Right: illustration of the energy transfer process (ET) from the CsPbBr$_3$ NCs to ML-MoSe$_2$ with enhanced carriers in the exciton continuum and trion formation. DDAB ligands are depicted as grey energy levels between the two materials.

between the source-drain electrodes to observe the light-induced change in conductivity. The basic structure of the system is illustrated by the cross-sectional schematic diagram depicted in **Figure 5a** and the optical micrograph of the system is shown in Figure S5, Supporting Information. The current-voltage (I_{SD}–V_{SD}) curves of the HET system were investigated both in dark and under non-polarized white light illumination

(active area ≈500 μm^2) at room temperature. The measurements were performed in a vacuum to avoid the influence of moisture and atmospheric gases and have been measured by varying V_{SD} up to 50 V. The comparison of the performance between ML-MoSe$_2$ and HET is described in Figure 5b. For both devices, I_{SD} is modulated by V_{SD}, both in dark and light conditions, indicating that I_{SD} can be effectively controlled by
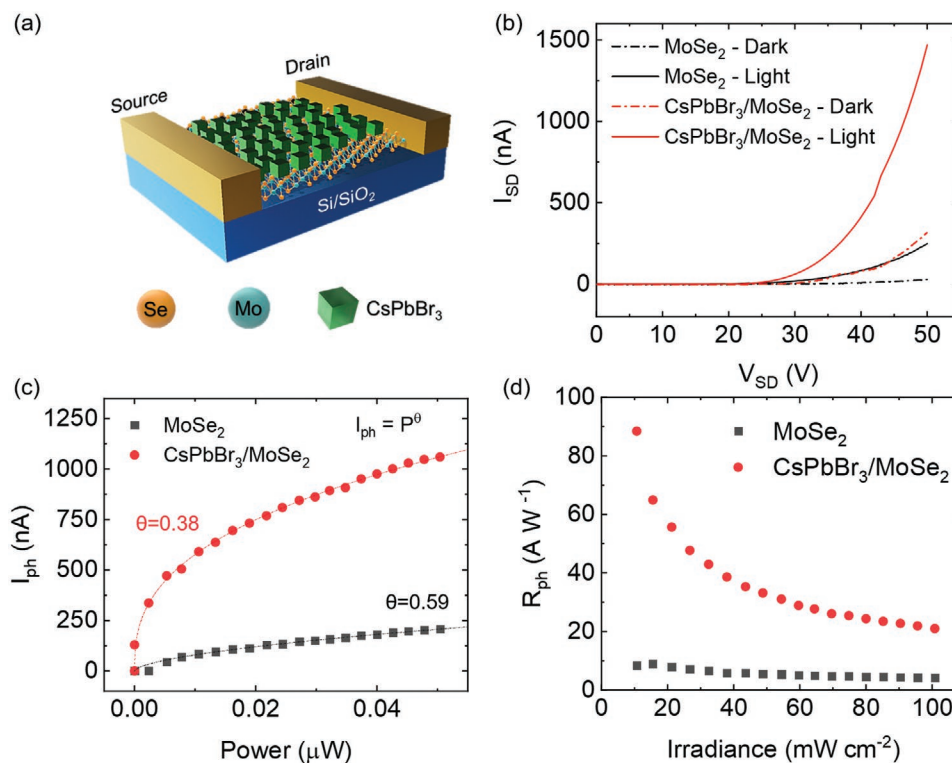

Figure 5. a) Schematic illustration of the CsPbBr$_3$/MoSe$_2$ (HET) proof of concept device structure. b) Source-drain current (I_{SD}) versus source-drain voltage (V_{SD}), both in dark and under white light conditions at bias voltages between 0 and 50 V. c) Photocurrent response for white incident light power on the active area of the devices. The dashed lines represent a power-law fit to the data. d) Photoresponsivity versus the irradiance curves.

**ADVANCED
SCIENCE NEWS**

www.advancedsciencenews.com

**ADVANCED
OPTICAL
MATERIALS**

www.advopticalmat.de

electrostatic doping. We observe that even in the dark the HET device outperforms the ML-MoSe$_2$ device by one order of magnitude (black curves in Figure 5b).

This can be explained by an improved transport of charges, induced by the contact of ML-MoSe$_2$ with the P-NCs. In general, current increase is attributed to an enhancement of the conductivity (defined as $\sigma \approx dI_{SD}/dV_{SD}$) due to the tuning of either mobility (μ_e) and/or carrier density n_e, as given by:[57]

$$\Delta\sigma \sim \Delta n_e \cdot \mu_e \qquad (5)$$

When the P-NCs get in touch with MoSe$_2$ it is conceivable that both μ_e and/or Δn_e are affected, as the interaction of the surface ligands of the P-NCs with ML-MoSe$_2$ might lead to the passivation of defects in the atomically thin 2D material, as shown also for other TMDC systems.[58–61] In fact, the defect passivation can induce a twofold enhancement of mobility in TMDCs due to the lowering of scattering centers, with a consequent increase in Δn_e up to 40 times.[58] While this can be an advantage for certain light-driven devices (e.g., solar cells), it might be detrimental for photodetector applications.

The $I_{SD}–V_{SD}$ curves for both samples were measured also under optical power illumination ($P_{ex} = 252$ µW). Notably, the photocurrent (I_{ph}) of the HET, defined as the difference between the current under a white light stimulus and the dark current (I_{dark}), is one order of magnitude (from 219 nA to 1156 nA for $V_{SD} = 50$ V, Figure 5b) higher than that of the pristine ML-MoSe$_2$ device. In dark conditions, the carriers are driven by an applied V_{SD}, hence a small I_{dark} flows across the device. Under light illumination, the absorbed photons generate electron-hole pairs that are separated and driven by the applied bias V_{SD} resulting in the observed photocurrent I_{ph}. We assume that the mobility μ_e of the channel material MoSe$_2$ in contact with the P-NCs is constant in dark and in light, as no chemical modification of the sample has been performed. Hence, the increase of σ is likely related to photogenerated excess carrier density Δn_e by one order of magnitude, giving another evidence of energy transfer from P-NCs. However, due to the complexity of analyzing optoelectronic systems, the exact quantification of the energy transfer process to the photocurrent generation is difficult, and we do not exclude a contribution also from the increased dark current. Subsequently, I_{ph} was measured under white light stimuli at different intensities over a range of optical powers from 10^{-5} to 10^{-4} W, as shown in Figure 5c. The presence of carrier generation, trapping, and recombination processes within the devices can be studied by the power dependence of the photodetector.[62] In an ideal photodetector, the photocurrent I_{ph} is proportional to the incident light power ($I \approx P^\theta$, with the power exponent $\theta = 1$). However, by fitting the curve with the aforementioned power law, in both cases of ML-MoSe$_2$ and HET, we found $\theta = 0.59$ and $\theta = 0.38$, respectively. This deviation from the unity value typically arises from the distribution of traps and recombination centers within the bandgap[63,64] and the saturation of these states under strong light excitation.[62,65–67] In order to estimate the light-detection performance of the two systems, the photoresponsivity (R_{ph}), defined as the efficiency in converting the optical signal into an electrical one, represents a fundamental figure of merit. We calculated R_{ph} of both devices given by:[62,65,68]

$$R_{ph} = \frac{I_{ph}}{I_r \cdot S} \qquad (6)$$

in which I_r is the irradiance, S is the active area of the device. We found that the maximum measured responsivity for both devices is achieved at the lowest irradiance (≈ 10 mW cm^{-2}) for both the ML-MoSe$_2$ device ($R_{ph} \approx 9$ A W^{-1}) and the HET device ($R_{ph} \approx 88$ A W^{-1}) and decreases with the increase of irradiation. The calculated R_{ph} values for HET are about one order of magnitude higher compared to the ML-MoSe$_2$-based device. The reason why R_{ph} exponentially decreases with the laser power increase could be related to the scattering due to defects and related recombination processes.[63,65,69,70] Taken all together, we were able to show that the HET device outperforms the ML-MoS$_2$ device by on the order of magnitude, hence exploiting the above-discussed effects related to the energy transfer.

3. Conclusion

To conclude, our HET of P-NCs/ML-MoSe$_2$ with a type I band alignment results into the efficient energy transfer from the nanocrystals to the MoSe$_2$. We observe the order of magnitude quenching of P-NC emission intensity and decay lifetime, and only minor enhancement in ML-MoSe$_2$ emission. We interpret these results as a direct energy transfer to the exciton continuum of MoSe$_2$ monolayers with the subsequent formation of free carriers and only a fraction recombining radiatively. We exploit this effect in a proof-of-concept heterostructure device, displaying order of magnitude enhancement of photocurrent. Taken together, in this work we identified a novel route to generate free carriers in MoSe$_2$ upon light absorption, avoiding the formation and subsequent dissociation of excitons with high binding energies in these materials. Hence, our results demonstrate new design opportunities for 2D-TMDC-based optoelectronic devices exploiting the direct generation of free carriers by energy transfer.

Supporting Information

Supporting Information is available from the Wiley Online Library or from the author.

Acknowledgements

Conflict of Interest

The authors declare no conflict of interest.

Data Availability Statement

Keywords

[1] K. F. Mak, C. Lee, J. Hone, J. Shan, T. F. Heinz, *Phys. Rev. Lett.* **2010**, *105*, 136805.

[2] Y. J. Zhang, R. N. Wang, G. Y. Dong, S. F. Wang, G. S. Fu, J. L. Wang, *AIP Adv.* **2019**, *9*, 125208.

[3] D. Andrzejewski, H. Myja, M. Heuken, A. Grundmann, H. Kalisch, A. Vescan, T. Kümmell, G. Bacher, *ACS Photonics* **2019**, *6*, 1832.

[4] D. Andrzejewski, E. Hopmann, M. John, T. Kümmell, G. Bacher, *Nanoscale* **2019**, *11*, 8372.

[5] H. G. Ji, P. Solís-Fernández, D. Yoshimura, M. Maruyama, T. Endo, Y. Miyata, S. Okada, H. Ago, *Adv. Mater.* **2019**, *31*, 1903613.

[6] M. Zulfiqar, Y. Zhao, G. Li, Z. C. Li, J. Ni, *Sci. Rep.* **2019**, *9*, 4571.

[7] A. Splendiani, L. Sun, Y. Zhang, T. Li, J. Kim, C.-Y. Chim, G. Galli, F. Wang, *Nano Lett.* **2010**, *10*, 1271.

[8] S. Roy, A. S. Sharbirin, Y. Lee, W. bin Kim, T. S. Kim, K. Cho, K. Kang, H. S. Jung, J. Kim, *Nanomaterials* **2020**, *10*, 1032.

[9] B. K. Choi, M. Kim, K. H. Jung, J. Kim, K. S. Yu, Y. J. Chang, *Nanoscale Res. Lett.* **2017**, *12*, 492.

[10] Y. H. Chang, W. Zhang, Y. Zhu, Y. Han, J. Pu, J. K. Chang, W. T. Hsu, J. K. Huang, C. L. Hsu, M. H. Chiu, T. Takenobu, H. Li, C. I. Wu, W. H. Chang, A. T. S. Wee, L. J. Li, *ACS Nano* **2014**, *8*, 8582.

[11] C. Xie, C. Mak, X. Tao, F. Yan, *Adv. Funct. Mater.* **2017**, *27*, 1603886.

[12] D. Kufer, G. Konstantatos, *ACS Photonics* **2016**, *3*, 2197.

[13] M. Massicotte, F. Vialla, P. Schmidt, M. B. Lundeberg, S. Latini, S. Haastrup, M. Danovich, D. Davydovskaya, K. Watanabe, T. Taniguchi, V. I. Fal'ko, K. S. Thygesen, T. G. Pedersen, F. H. L. Koppens, *Nat. Commun.* **2018**, *9*, 1633.

[14] C. Zhang, Y. Zhang, Z. Fang, Y. Chen, Z. Chen, H. He, H. Zhu, *ACS Appl. Mater. Interfaces* **2021**, *13*, 41895.

[15] Q. Fang, Q. Shang, L. Zhao, R. Wang, Z. Zhang, P. Yang, X. Sui, X. Qiu, X. Liu, Q. Zhang, Y. Zhang, *J. Phys. Chem. Lett.* **2018**, *9*, 1655.

[16] X. Song, X. Liu, D. Yu, C. Huo, J. Ji, X. Li, S. Zhang, Y. Zou, G. Zhu, Y. Wang, M. Wu, A. Xie, H. Zeng, *ACS Appl. Mater. Interfaces* **2018**, *10*, 2801.

[17] H. Li, X. Zheng, Y. Liu, Z. Zhang, T. Jiang, *Nanoscale* **2018**, *10*, 1650.

[18] Y. Yu, Y. Zhang, X. Song, H. Zhang, M. Cao, Y. Che, H. Dai, J. Yang, H. Zhang, J. Yao, *ACS Photonics* **2017**, *4*, 950.

[19] Z. Song, Y. Wang, Y. Zhu, P. Bai, A. Hu, Y. Gao, *J. Semicond.* **2021**, *42*, 082901.

[20] M. S. Hassan, P. Basera, S. Bera, M. Mittal, S. K. Ray, S. Bhattacharya, S. Sapra, *ACS Appl. Mater. Interfaces* **2020**, *12*, 7317.

[21] M. de Franco, M. Cirignano, T. Cavattoni, H. Bahmani Jalali, M. Prato, F. di Stasio, *Opt. Mater.: X* **2022**, *13*, 100124.

[22] M. Imran, P. Ijaz, D. Baranov, L. Goldoni, U. Petralanda, Q. Akkerman, A. L. Abdelhady, M. Prato, P. Bianchini, I. Infante, L. Manna, *Nano Lett.* **2018**, *18*, 7822.

[23] F. Liu, W. Wu, Y. Bai, S. H. Chae, Q. Li, J. Wang, J. Hone, X. Y. Zhu, *Science* **2020**, *367*, 903.

[24] C. Trovatello, A. Marini, X. Xu, C. Lee, F. Liu, N. Curreli, C. Manzoni, S. Dal Conte, K. Yao, A. Ciattoni, J. Hone, X. Zhu, P. J. Schuck, G. Cerullo, *Nat. Photonics* **2020**, *15*, 6.

[25] M. Velický, G. E. Donnelly, W. R. Hendren, S. McFarland, D. Scullion, W. J. I. DeBenedetti, G. C. Correa, Y. Han, A. J. Wain, M. A. Hines, D. A. Muller, K. S. Novoselov, H. D. Abruńa, R. M. Bowman, E. J. G. Santos, F. Huang, *ACS Nano* **2018**, *12*, 10463.

[26] D. H. Kang, S. G. Kim, Y. C. Kim, I. T. Han, H. J. Jang, J. Y. Lee, N. G. Park, *ACS Energy Lett.* **2020**, *5*, 2191.

[27] H. L. Liu, T. Yang, J. H. Chen, H. W. Chen, H. Guo, R. Saito, M. Y. Li, L. J. Li, *Sci. Rep.* **2020**, *10*, 15282.

[28] J. Kang, S. Tongay, J. Zhou, J. Li, J. Wu, *Appl. Phys. Lett.* **2013**, *102*, 012111.

[29] A. A. Lutich, G. Jiang, A. S. Susha, A. L. Rogach, F. D. Stefani, J. Feldmann, *Nano Lett.* **2009**, *9*, 2636.

[30] J. R. Lakowicz, *Principles of Fluorescence Spectroscopy*, Springer, New York **2006**.

[31] S. Koley, J. Cui, Y. E. Panfil, U. Banin, *Acc. Chem. Res.* **2021**, *54*, 1178.

[32] J. T. Dubose, P. v. Kamat, *J. Am. Chem. Soc.* **2021**, *143*, 19214.

[33] A. Sillen, Y. Engelborghs, *Photochem. Photobiol.* **1998**, *67*, 475.

[34] M. Imran, P. Ijaz, L. Goldoni, D. Maggioni, U. Petralanda, G. Almeida, I. Infante, L. Manna, *ACS Energy Lett.* **2019**, *4*, 819.

[35] Z. Y. Zhang, H. Y. Wang, Y. X. Zhang, Y. W. Hao, C. Sun, Y. Zhang, B. R. Gao, Q. D. Chen, H. B. Sun, *Sci. Rep.* **2016**, *6*, 27286.

[36] N. Geva, J. J. Shepherd, L. Nienhaus, M. G. Bawendi, T. van Voorhis, *J. Phys. Chem. C* **2018**, *122*, 26267.

[37] J. H. Park, A.-Y. Lee, J. C. Yu, Y. S. Nam, Y. Choi, J. Park, M. H. Song, **2019**, *11*, 8424.

[38] M. Chidambaram, S. U. Sonavane, J. de la Zerda, Y. Sasson, *Tetrahedron* **2007**, *63*, 7696.

[39] D. Kozawa, R. Kumar, A. Carvalho, K. K. Amara, W. Zhao, S. Wang, M. Toh, R. M. Ribeiro, A. H. Castro Neto, K. Matsuda, G. Eda, **2014**, *5*, 4543.

[40] L. Yuan, L. Huang, *Nanoscale* **2015**, *7*, 7402.

[41] K. F. Mak, K. He, C. Lee, G. H. Lee, J. Hone, T. F. Heinz, J. Shan, *Nat. Mater.* **2012**, *12*, 207.

[42] E. Courtade, M. Semina, M. Manca, M. M. Glazov, C. Robert, F. Cadiz, G. Wang, T. Taniguchi, K. Watanabe, M. Pierre, W. Escoffier, E. L. Ivchenko, P. Renucci, X. Marie, T. Amand, B. Urbaszek, *Phys. Rev. B* **2017**, *96*, 085302.

[43] Z. Luo, H. Jia, L. Lv, Q. Wang, X. Yan, *Nanoscale* **2020**, *12*, 17754.

[44] A. Arora, T. Deilmann, T. Reichenauer, J. Kern, S. Michaelis De Vasconcellos, M. Rohlfing, R. Bratschitsch, *Phys. Rev. Lett.* **2019**, *123*, 167401.

[45] I. Kriegel, M. Ghini, S. Bellani, K. Zhang, A. W. Jansons, B. M. Crockett, K. M. Koskela, E. S. Barnard, E. Penzo, J. E. Hutchison, J. A. Robinson, L. Manna, N. J. Borys, P. J. Schuck, *J. Phys. Chem. C* **2020**, *124*, 8000.

[46] M. Ghini, E. S. Yanev, C. Kastl, K. Zhang, A. W. Jansons, B. M. Crockett, K. M. Koskela, E. S. Barnard, E. Penzo, J. E. Hutchison, J. A. Robinson, L. Manna, N. J. Borys, P. J. Schuck, I. Kriegel, *Adv. Photonics Res.* **2021**, *2*, 2000151.

[47] J. Duan, P. Chava, M. Ghorbani-Asl, D. Erb, L. Hu, A. v. Krasheninnikov, H. Schneider, L. Rebohle, A. Erbe, M. Helm, Y. J. Zeng, S. Zhou, S. Prucnal, *Adv. Funct. Mater.* **2021**, *31*, 2104960.

[48] J. S. Ross, S. Wu, H. Yu, N. J. Ghimire, A. M. Jones, G. Aivazian, J. Yan, D. G. Mandrus, D. Xiao, W. Yao, X. Xu, *Nat. Commun.* **2013**, *4*, 1474.

[49] S. Mouri, Y. Miyauchi, K. Matsuda, *Nano Lett.* **2013**, *13*, 5944.

[50] J. Siviniant, D. Scalbert, A. v. Kavokin, D. Coquillat, J. P. Lascaray, *Phys. Rev. B* **1999**, *59*, 1602.

[51] X. Xu, Q. Zhang, J. Zhang, *J. Phys.: Condens. Matter* **2003**, *15*, R471.

[52] H. Yang, K. Wei, J. Jiang, X. Cheng, Y. Liu, *Appl. Opt.* **2016**, *55*, 6321.

[53] A. O. A. Tanoh, J. Alexander-Webber, J. Xiao, G. Delport, C. A. Williams, H. Bretscher, N. Gauriot, J. Allardice, R. Pandya,

Y. Fan, Z. Li, S. Vignolini, S. D. Stranks, S. Hofmann, A. Rao, *Nano Lett.* **2019**, *19*, 6299.

[54] S. Tongay, J. Suh, C. Ataca, W. Fan, A. Luce, J. S. Kang, J. Liu, C. Ko, R. Raghunathanan, J. Zhou, F. Ogletree, J. Li, J. C. Grossman, J. Wu, *Sci. Rep.* **2013**, *3*, 2657.

[55] Y. Kwon, K. Kim, W. Kim, S. Ryu, H. Cheong, *Curr. Appl. Phys.* **2018**, *18*, 941.

[56] N. Lundt, E. Cherotchenko, O. Iff, X. Fan, Y. Shen, P. Bigenwald, A. v. Kavokin, S. Höfling, C. Schneider, *Appl. Phys. Lett.* **2018**, *112*, 031107.

[57] N. W. Ashcroft, N. D. Mermin, *Solid State Physics*, Holt-Saunders, London **1976**.

[58] J. Jiang, T. Xu, J. Lu, L. Sun, Z. Ni, *Research* **2019**, *2019*, 4641739.

[59] G. Wu, R. Liang, M. Ge, G. Sun, Y. Zhang, G. Xing, *Adv. Mater.* **2022**, *34*, 2105635.

[60] M. Amani, D. H. Lien, D. Kiriya, J. Xiao, A. Azcatl, J. Noh, S. R. Madhvapathy, R. Addou, K. C. Santosh, M. Dubey, K. Cho, R. M. Wallace, S. C. Lee, J. H. He, J. W. Ager, X. Zhang, E. Yablonovitch, A. Javey, *Science* 1979 **2015**, *350*, 1065.

[61] S. Zhang, X. Wang, Y. Chen, G. Wu, Y. Tang, L. Zhu, H. Wang, W. Jiang, L. Sun, T. Lin, H. Shen, W. Hu, J. Ge, J. Wang, X. Meng, J. Chu, *ACS Appl. Mater. Interfaces* **2019**, *11*, 23667.

[62] H. Fang, W. Hu, H. Fang, W. Hu, *Adv. Sci.* **2017**, *4*, 1700323.

[63] X. Zhang, J. Jie, W. Zhang, C. Zhang, L. Luo, Z. He, X. Zhang, W. Zhang, C. Lee, S. Lee, *Adv. Mater.* **2008**, *20*, 2427.

[64] B. Mukherjee, Y. Cai, H. R. Tan, Y. P. Feng, E. S. Tok, C. H. Sow, *ACS Appl. Mater. Interfaces* **2013**, *5*, 9594.

[65] J. Ghosh, P. K. Giri, *J. Physics: Mater.* **2021**, *4*, 032008.

[66] N. Nagaosa, Y. Tokura, *Nat. Nanotechnol.* **2013**, *8*, 899.

[67] O. Lopez-Sanchez, D. Lembke, M. Kayci, A. Radenovic, A. Kis, *Nat. Nanotechnol.* **2013**, *8*, 497.

[68] N. Curreli, M. Serri, M. I. Zappia, D. Spirito, G. Bianca, J. Buha, L. Najafi, Z. Sofer, R. Krahne, V. Pellegrini, F. Bonaccorso, *Adv. Electron. Mater.* **2021**, *7*, 2001080.

[69] D. S. Schulman, A. J. Arnold, S. Das, *Chem. Soc. Rev.* **2018**, *47*, 3037.

[70] Y. Liu, J. Guo, E. Zhu, L. Liao, S. J. Lee, M. Ding, I. Shakir, V. Gambin, Y. Huang, X. Duan, *Nature* **2018**, *557*, 696.